Advances in Science and Technology Research Journal

Advances in Science and Technology Research Journal, 2026, 20(5), 437–454
https://doi.org/10.12913/22998624/216702
ISSN 2299-8624, License CC-BY 4.0

Received: 2025.02.12
Accepted: 2026.03.16
Published: 2026.04.01

Higher-order finite element implementation of non-axisymmetric thermoelastic analysis in functionally graded material cylinder

Heba Al Zoubi[1], Sameh Alsaqoor[2*], Ibrahim Abu Al-Shaikh[1], Gabriel Borowski[3], Nabil Beithou[2]

[1] Mechanical Engineering Department, University of Jordan, Amman, Jordan
[2] Mechanical Engineering Department, Tafila Technical University, Tafila, Jordan.
[3] Faculty of Environmental Engineering and Energy, Lublin University of Technology, Lublin, Poland
* Corresponding author's e-mail: sameh@ttu.edu.jo

ABSTRACT

Finite element solutions are highly sensitive to the finite element shape selected and the number of nodes. In this study, a new higher-order finite element analysis is employed to investigate the non-axisymmetric thermoelastic performance of a hollow cylinder made of functionally graded material (FGM) exposed to variable hoop temperature. The analysis employs higher-order finite triangular elements with 6 and 10-nodes to increase the accuracy of the numerical solution as it deals with a curve shaped problem. A strong agreement was achieved when a comprehensive comparison of the thermal and displacement distributions across the cylinder's annulus was conducted with analytical and numerical solutions from prior literature. This study also examines the impact of the volume-graded index on heat and displacement variations along the radial direction, i.e., as the volume exponent index increases, the radial displacement decreases. This investigation contributes to highlighting the effectiveness of the finite element method in analyzing complex thermoelastic systems. Furthermore, when the heat distribution and radial displacement components follow harmonic patterns like sine, the circumferential displacement behaves in the opposite direction, like cosine. Moreover, the results of the implementation of the higher-order triangular element in non-axisymmetric problems will improve and enhance the results of the temperature and displacement components. The results further show that the higher order of triangular elements obtains closure results to reach some available special analytical solutions.

Keywords: functionally graded materials; non-axisymmetric thermoelastic behavior; finite element analysis; hollow cylinder.

INTRODUCTION

Cylinder structures with their different applications are found in various component structural and device systems, such as aerospace, submarine structures, vessels, pipes, sensors, and pneumatic systems. Cylinder structures are often subjected to constant or cycling high pressures and temperatures so that thermal stresses are induced. These structures are manufactured and designed using metal alloys or advanced materials such as composites and functionally graded materials (FGMs). The cylindrical structures that are made of composite materials have many pros properties, which are made by combining two or more materials in a microscopic form, and their elements do not dissolve or fuse into each other. However, some layered composite cylinders subjected to impact load or repeated stress cycles cause a delamination phenomenon that is defined as a separation of layers and weakness at interfaces between the neighboring layers.

The solution to avoid these problems and overcome rapid changes in material properties is by utilizing the FGMs discovered in 1984 by a Japanese research group Dai et al. (2016). Paul et al. (2022) conducted a study on the analysis of steady-state elastic stresses in thick hollow axisymmetric cylinders made of FGM. These cylinders were subjected to internal and external pressure conditions, and the analysis was carried out using an iteration technique along with the finite element method (FEM). Furthermore, they examined a functionally graded cylinder with specialized material properties. Young's Modulus is taken to vary exponentially from the inner to the outer radius of the cylinder. Nayak et al. (2019) illustrated the elastoplastic analysis of functionally graded disks under centrifugal and thermal loads in the post-elastic phase. They characterized the FGM with a seamless supply of ceramic and metal components laterally the radial axis, utilizing a power law for volume fraction difference. The governing equations in the post-elastic phase were derived through the smallest total potential energy within Hencky's deformation theory of plasticity. Dai et al. (2016) studied thermal stresses induced in the FGM cylinders that are exposed to high pressure and temperature, which significantly depress the strength and functionality.

Many researchers have studied the behavior of thermoelastic FGM hollow structures that are subjected to one-dimensional (1D) and two-dimensional (2D) axisymmetric or asymmetric thermal and mechanical loads. Analytical or numerical techniques like finite difference (FD) or FEMs were applied to solve such problems. Few researchers focus on studying the non-axisymmetric thermoelastic study of functionally graded hollow cylinders under asymmetric thermal and mechanical loads, where the temperature and pressure distributions are assumed to be functional in the circumferential direction. Therefore, the problem becomes plane-strain with infinite-length cylinders under non-axisymmetric loading conditions. The functionally graded cylinders have been performed on variational properties that are varied continuously, which are expressed by an exponential, power, or mixture law in a thickness direction. Benslimane et al. (2023) investigated the stress analysis of a rotating thick-walled nonhomogeneous sphere made of FGM, which experiences internal and/or external pressure along with thermal loading. They employed three-dimensional elasticity theory for their analysis. The study assumed that the mechanical and thermal properties vary throughout the FGM thickness according to a nonlinear power law expression for a constant value of Poisson's ratio. Farukoğlu et al. (2023) involve an internally pressurized disk with variable thickness and power-law graded material. This approach extends the power-law concept for Young's modulus and Poisson's ratio of the graded material in the radial direction. As a result, the solution involves various Bessel functions.

Sreeju Nair and Pany (2020) showed the overview of FGM basic concepts, classification, properties, and its modeling, which may focus on the static and dynamic analysis of functionally graded panels. They assumed that the material properties of FGM for the panel are graded in the thickness direction according to the power-law distribution of volume fractions of the constituents. Shao et al. (2008) studied the unsteady-state thermo-mechanical problem of FGM hollow circular cylinders. They assumed that the material properties of FGM are temperature-independent and vary exponentially in the radial direction. Yıldırım (2017) studied both spherical and cylindrical vessels that are made of non-homogeneous radially varied FGMs.

Two-dimensional FGM was the attention of Eldeeb et al. (2023), investigated the thermoelastic stress analysis of a 2D-FGM cylinder exposed to symmetric or asymmetric thermal loading. They assumed variations in material properties occurring simultaneously in both radial and tangential directions. Tang and Ma (2024) presented the descriptions of heat transfer and thermal analysis within mechanical designs using computational fluid dynamics (CFD) tools. It is assumed CF modeling is capable of evaluating all heat transfer mechanisms: conduction, convection, and radiation, with predictions on temperature distributions in solid embodiment or fluids. Golzari and Asgari (2018) studied the power-law function of a 2D thick hollow FGM cylinder in polar coordinates. Asgari and Akhlaghi

(2009) investigated the effects of 2D that were expressed in a power-law function on the distributions of temperature, displacements, and stress components through the FGM cylinder.

Salehi and Ahmadi (2022) investigated the transient thermoelastic axisymmetric response of 2D-FG thick hollow cylinders with material properties graded in both radial and axial directions. They introduced a meshless local Petrov-Galerkin formulation to discretize the linear equations of the 2D-FG cylinder. Eldeeb et. al. (2021) observed the thermos-elastoplastic conduct of a rotating multilayer cylinder made of temperature-dependent FGM using an FD approach. Each layer was regarded as a compound with constant volume fractions. Eldeeb et al. (2020) investigated the thermo-elastoplastic performances of rotating discs with non-uniform thickness, made of FGM employing the FD method. The sandwich disc comprises multiple layers of equal width with unique volume fractions and temperature-dependency of the integral materials. Saadatfar (2022) illustrated the distribution of temperature and moisture within a cylinder made of FGM under transient hydrothermal conditions. The solution involved using the Fourier series expansion, lengthways the differential quadrature, and Newmark's methods in the time domain. Shariyat (2009) studied the nonlinear thermoelastic analysis of thick FG cylindrical vessels employing the numerical Laplace transform to find the values of temperature and thermal stress. Singh et al. (2024) investigated the elastic stress and deformation analysis of a hollow disk subjected to various conditions, including rotation, gravity, internal pressure, and temperature fluctuations. Sharma and Kaur (2020) conducted a numerical study on the stress field in FGM hollow cylinders using FEM. The FGM cylinder was exposed to internal pressure and uniform heat generation. The material properties of the FGM cylinder were supposed to vary exponentially laterally across the cylinder's radius.

Jabbari et al. (2009) established an exact solution of two-dimensional axisymmetric stresses for a cylinder through FGM. Hosseini et. al. (2006) examined analytically special nonlinear heat conduction problems in an FGM cylindrical shell. Benslimane and Methia (2018) proposed analytical and FE solutions for estimating the thermal and elastic analysis in the radial direction of an FGM thick-walled cylinder under uniform internal and external pressures. Pany and Parthan (2001) studied vibration-induced fatigue and excessive noise radiation that are serious problems of periodically supported curved panels by using high-precision triangular finite elements to determine multi-supported curved panel frequencies.

The thermo-elastic performance of FGM hollow cylinders that are exposed to non-axisymmetric thermomechanical loads was investigated by many researchers. Paul and Sahni (2021) examined the assessment of mechanical stress in functionally graded cylinders under non-axisymmetric loading conditions. They utilized the Fourier half-range series and Euler differential equations as analytical tools. Jabbari et al. (2003) analyzed two-dimensional steady-state thermal stresses for an FGM hollow thick cylinder. The temperature was spreading, and thermal and mechanical boundary settings were determined on the inner and outer surfaces. Xie et al. (2013) utilized Newmark's method to investigate the asymmetrical thermoelastic dynamic behavior of the FGM hollow cylinder that was exposed to asymmetrical loads. Asgari and Akhlaghi (2009) dealt with a 2D-FG hollow cylinder under steady-state thermal and mechanical loads. They used axisymmetric ring FE to solve the thermoelasticity equations. Shojaeefard and Najibi (2017) investigated the thick hollow 2D–FGM by employing weighted residual FEM to discretize the domain.

Few researchers covered the part of analyzing non-axisymmetric FGM hollow cylinders by using rectangular cross-section elements with higher-order Lagrange shape functions. On the other hand, none of the researchers have used the higher-order triangular elements. Najibi and Talebitooti (2017) studied the behavior of transient thermoelastic of a 2D-FGM hollow cylinder by applying the higher order of Lagrange FEM. This paper focuses on applying FEM using higher-order triangular elements employed to solve the functionally graded hollow cylinder exposed to non-axisymmetric thermo-elastic loads.

Basic governing equations

Consider the FGM hollow cylinder characterized by an inner radius r_i, an outer radius r_o, and a power index n, exposed to non-axisymmetric thermo-mechanical loads, Figure 1. The geometry of the FGM hollow cylinder relative with the polar coordinate system (r, θ).

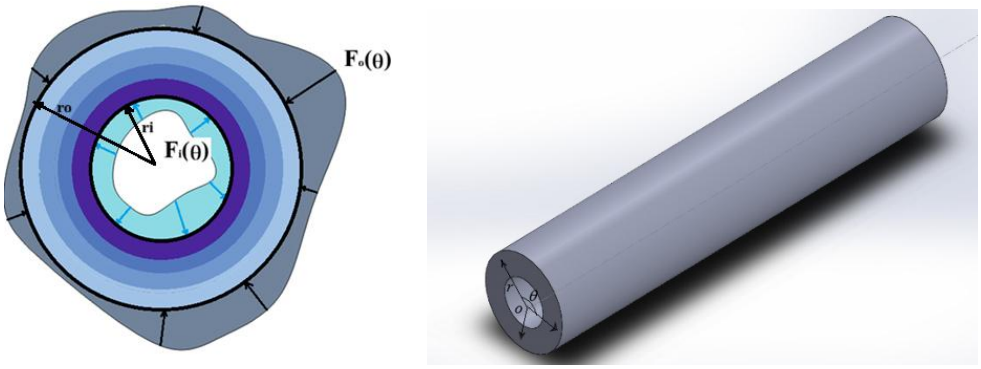

Figure 1. The FGM hollow cylinder in (r, θ, z)-coordinate

The steady-state heat transmission equation for FGM cylinder under non-axisymmetric conditions, temperature distributions in polar coordinates, no heat generation, and radial grading of material properties, can be formulated as:

$$\frac{1}{r}\frac{\partial}{\partial r}\left(r\ k_r(r)\frac{\partial T\ (r,\theta)}{\partial r}\right)+\frac{1}{r^2}\frac{\partial}{\partial \theta}\left(k_\theta\ (r)\frac{\partial T\ (r,\theta)}{\partial \theta}\right)=0$$
$$C_{11}T(r_i,\theta)=\zeta_i(\theta), \tag{1}$$
$$C_{21}T(r_o,\theta)=\zeta_o(\theta)$$

where: $T = T(r, \theta)$ represents the temperature as a function of r $(r_i < r \leq r_o)$ and θ $(-\pi \leq \theta \leq \pi)$ inside the cylinder, $k_r = k_\theta = k$ are the thermal conductivities, and C_{11}, C_{21} are the coefficients of conduction. Further, the functions $\zeta_i(\theta)$ and $\zeta_o(\theta)$ are known functions of θ and assumed on the inner and outer surface of the hollow cylinder, respectively.

In non-axisymmetric plane-strain problems, the strain-displacement relations can be expressed in a polar coordinate system as Jabbari et. al. (2003):

$$\varepsilon_{rr}=\frac{\partial u}{\partial r},\quad \varepsilon_{\theta\theta}=\frac{1}{r}\left(\frac{\partial v}{\partial \theta}+u\right),\quad \varepsilon_{r\theta}=\frac{1}{2}\left(\frac{1}{r}\frac{\partial u}{\partial \theta}+\frac{\partial v}{\partial r}-\frac{v}{r}\right) \tag{2}$$

The stress-strain relations in non-axisymmetric plane-strain problems are expressed in matrix form as, Logan (2017):

$$\begin{Bmatrix}\sigma_{rr}\\ \sigma_{\theta\theta}\\ \tau_{r\theta}\end{Bmatrix}=\begin{bmatrix}c_{11} & c_{12} & 0\\ c_{21} & c_{22} & 0\\ 0 & 0 & c_{33}\end{bmatrix}\begin{bmatrix}\varepsilon_{rr}\\ \varepsilon_{\theta\theta}\\ \varepsilon_{r\theta}\end{bmatrix}-c_T\left\{T^e\right\} \tag{3}$$

where: ε_{rr}, $\varepsilon_{\theta\theta}, \varepsilon_{r\theta}$ are the normal and shear strain, and σ_{rr}, $\sigma_{\theta\theta}$, $\tau_{r\theta}$ are the normal and shear stresses, respectively.

In addition, the coefficients c_{ij} 's are defined in terms of the material properties as:

$$c_{11}=c_{22}=\frac{(1-\upsilon)E(r)}{(1+\upsilon)(1-2\upsilon)},\ c_{12}=c_{21}=\frac{\upsilon E(r)}{(1+\upsilon)(1-2\upsilon)},$$
$$c_{33}=\frac{E(r)}{2(1+\upsilon)},\ c_T=\frac{E(r)\alpha(r)}{1-2\upsilon} \tag{4}$$

The equilibrium equations, by disregarding body forces, can be formulated as:

$$\frac{\partial\sigma_{rr}}{\partial r}+\frac{1}{r}\frac{\partial\tau_{r\theta}}{\partial\theta}+\frac{\sigma_{rr}-\sigma_{\theta\theta}}{r}=0,$$
$$\frac{1}{r}\frac{\partial\sigma_{\theta\theta}}{\partial\theta}+\frac{\partial\tau_{r\theta}}{\partial r}+\frac{2\tau_{r\theta}}{r}=0 \tag{5}$$

Material properties

A long 1D-FGM hollow cylinder, the material constituent is made of (Si_3N_4) as a ceramic and (SUS_304) as a metal. The cylinder's material is assumed to be graded along the *r*-direction, has ceramic at its inner radius and metals at its outer radius. The material properties of the structure are taken as shown in Table 1.

Table 1. The materials properties of the FGM hollow cylinder (Xie et al., 2013)

Material	Material properties	Symbol	Unit	Value
Si_3N_4	Young's modulus	E	GPa	348.43
	Coefficient of thermal expansion	α	1/K	5.87×10^{-6}
	Thermal conductivity	k	W/mK	13.72
	Density	ρ	kg/m^3	2370
SUS_304	Young's modulus	E	GPa	201.04
	Coefficient of thermal expansion	α	1/K	12.33×10^{-6}
	Thermal conductivity	k	W/mK	15.38
	Density	ρ	kg/m^3	8166

The material of the FGM cylinder is supposed to be graded continuously through the *r*-direction. Thus, the volume fraction of the ceramic material changes from 100% at the inner surface of the FGM hollow cylinder to 0% at the outer surface, whereas the volume fraction of metal changes from 100% at the outer surface to 0% at the inner surface. The varying volume fraction of materials using by power-law expression, as shown in Darabseh et al. (2013):

$$P(r)=(P_i-P_o)\left[1-\left(\frac{r-r_i}{r_o-r_i}\right)^n\right]+P_o \tag{6}$$

where: $P(r)$ – the mechanical and thermal properties of FGM, as functions of grading direction, except the Poisson's ratio. The subscripts i and o denote the properties corresponding to the inner and outer surfaces, respectively. The grading parameter n ($0<n\leq\infty$) represents the volume exponent index.

Finite element modeling

To solve the equations describing the example of a hollow cylinder, the problem is discretized by 2D triangular elements to idealize the domain. The temperature field within each element can be described in terms of the shape functions and nodal temperature as:

$$T(r,\theta)=\sum_{i=1}^{m} S_i(r,\theta)\ T^e=\{S\}\{T^e\} \tag{7}$$

where: $\{S\}$ represents the row matrix of the shape functions, and $\{T^e\}$ signifies the nodal temperature column matrix, m denotes the node number assigned to the selected element.

The process of generating shape functions for a triangular element with 6 and 10-nodes from an (m–1) order polynomial can be described directly using the 2D Lagrange polynomial formula, which is adapted to a polar coordinate system to indicate the location of each node X_i

$$S_J=\prod_{\substack{M=1\\J\neq M}}^{n} a_1\frac{(X-X_M)}{(X_J-X_M)}=\frac{(X-X_1)(X-X_2)...(X-X_n)}{(X_J-X_1)(X_J-X_2)...(X_J-X_n)} \tag{8}$$

Applying the principle of minimum potential energy method, the potential energy function π_h is expressed as:

$$\pi_h=U+\Omega_q+\Omega_h+\Omega_Q+\Omega_r \tag{9}$$

where

$$U=\frac{1}{2}\int_V\left[\frac{1}{r}\frac{\partial}{\partial r}\left(r\,k_r(r)\frac{\partial T(r,\theta)}{\partial r}\right)+\frac{1}{r^2}\frac{\partial}{\partial\theta}\left(k_\theta(r)\frac{\partial T(r,\theta)}{\partial\theta}\right)\right]dV,$$

$$\Omega_q=\int_{\Gamma_1} f_{bound}\ \{T^e\}\,d\Gamma,\quad \Omega_h=\frac{1}{2}\int_{\Gamma_2} h\,(T-T_\infty)^2\,d\Gamma,$$

$$\Omega_Q=-\int_V \dot{g}\,dV,\quad \Omega_r=\int_{\Gamma_3} h_r\,(T^4-T_\infty^4)\,d\Gamma,$$

where: $S_{f_{bound}}$ – the area of heat flux f_{bound}, S_{cv} – the area of convection losses $h(T-T_\infty)$.

Not specified Ω_q and Ω_h on the same surface because they cannot occur on it at the same time. It was assumed that there is no heat generation, heat flux into the domain, or heat losses by convection and radiation heat transfer are specified on the boundaries. On minimizing Eq. (9) with respect to $\{T^e\}$ one can write:

$$\begin{aligned}\frac{\partial\pi_h}{\partial\{T^e\}}&=\int_V[B]^T[D][B]dV\ \{T^e\}+\int_V h\{N\}^T\{N\}dS\,\{T^e\}\\&-\int_V\{N\}^T\dot{g}\,dV-\int_{S_{f_{bound}}}\{N\}^T f_{bound}\,dS-\int_{S_{cv}} h\{N\}^T T_\infty dS\end{aligned} \tag{10}$$

where: $[B]_{2\times 2m}$ is obtained by differentiating $T(r,\theta)$ in Eq. (7) with respect to r and θ, $[D]$ is the material property matrix, and $[K_e]$ represents the element stiffness matrix that can be defined as:

$$[K_e]=\int_V[B]^T[D][B]dV,\quad [B]=\begin{Bmatrix}\dfrac{\partial\sum_{i=1}^{n}S_i}{\partial r}\\[2ex]\dfrac{\partial\sum_{i=1}^{n}S_i}{\partial\theta}\end{Bmatrix},\quad [D]=\begin{bmatrix}k(r) & 0\\ 0 & \dfrac{1}{r^2}k(r)\end{bmatrix} \tag{11}$$

The assumption regarding the force elemental matrix terms indicating temperature at the inner and outer surfaces was expressed by:

$$\left\{F_i^e\right\} = \int_{\Gamma} T\left(r_i, \theta\right) d\theta$$
$$\left\{F_o^e\right\} = \int_{\Gamma} T\left(r_o, \theta\right) d\theta \tag{12}$$

The global matrix equations and the boundary conditions matrix are assembled by assembling the element equations in Eq. (10):

$$\left[K\right]^G \left\{T\right\} = \left\{F\right\}^G$$
$$\left[K\right]^G = \sum_{i=1}^{NE} \left[K_{e(i)}\right], \quad \left\{F\right\}^G = \sum_{i=1}^{NE} \left[F_{(i)}^e\right] \tag{13}$$

where: NE is the total number of elements in the entire structure.

The first equation provided in (13) can be rearranged into its final form as:

$$\left[\left[K\right]^G \quad \left[-I\right]\right]_{N\times 2N} \begin{Bmatrix} \{T\} \\ \{F\}^G \end{Bmatrix}_{2N\times 1} = \{0\}_{N\times 1} \tag{14}$$

where: $[I]$ is the identity matrix, $\{0\}$ is the zero vector, and N is the number of nodes in the global matrix.

The boundary conditions can be written as:

$$\left[\left[X_1\right] \quad \left[X_2\right]\right]_{N\times 2N} \begin{Bmatrix} \{T\} \\ \{F\}^G \end{Bmatrix}_{2N\times 1} = \left\{\varphi\right\}_{N\times 1} \tag{15}$$

where: $\left[X_1\right]$, $\left[X_2\right]$ are suitable matrices satisfying the assumed boundary conditions related to nodal temperature. Both the stiffness matrix and boundary conditions can be satisfied by employing:

$$\begin{bmatrix} \left[K\right]^G & \left[-I\right] \\ \left[X_1\right] & \left[X_2\right] \end{bmatrix}_{2N\times 2N} \begin{Bmatrix} \{T\} \\ \{F\}^G \end{Bmatrix}_{2N\times 1} = \begin{Bmatrix} \{O\} \\ \{\varphi\} \end{Bmatrix}_{2N\times 1} \tag{16}$$

The linear algebraic system presented in Eq. (16) can be employed to address non-axisymmetric heat transfer problems, accommodating various force and temperature conditions in polar coordinates. For example, shape functions for a typical triangular element with 6 nodes can be derived as Figure 2.

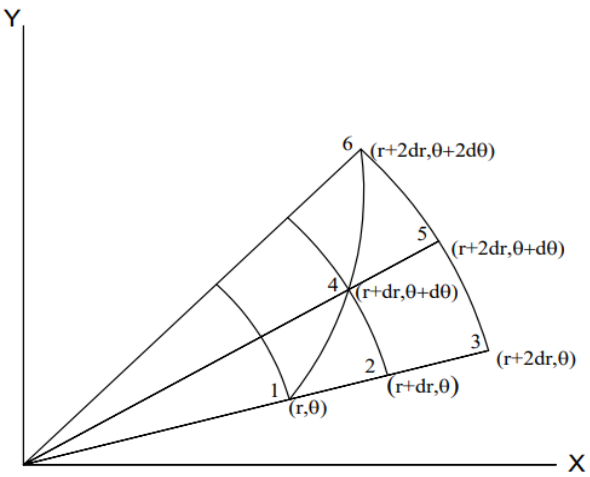

Figure 2. Typical triangular element with 6-nodes

$$
\begin{aligned}
S_1(r,\theta) &= A_1\left(r-r_2\right)\left(r-r_3\right)\\
S_2(r,\theta) &= A_2\left(r-r_1\right)\left(r-r_3\right)\left(\theta-\theta_4\right)\\
S_3(r,\theta) &= A_3\left(r-r_1\right)\left(r-r_2\right)\left(\theta-\theta_5\right)\left(\theta-\theta_6\right)\\
S_4(r,\theta) &= A_4\left(r-r_1\right)\left(r-r_3\right)\left(\theta-\theta_2\right)\\
S_5(r,\theta) &= A_5\left(r-r_1\right)\left(r-r_2\right)\left(\theta-\theta_3\right)\left(\theta-\theta_6\right)\\
S_6(r,\theta) &= A_6\left(r-r_1\right)\left(r-r_2\right)\left(\theta-\theta_2\right)\left(\theta-\theta_5\right)
\end{aligned}
\tag{17}
$$

Non-axisymmetric plane strain equations are solved by using higher-order triangular elements featuring 6 and 10-nodes through a variational approach to derive a finite element formulation. The nodal displacements and the generalized displacement function within an element "e" can be delineated as:

$$
\begin{aligned}
\left\{d^{(e)}\right\} &= \begin{Bmatrix} u_j \\ v_j \end{Bmatrix}, \quad j = 1 \ldots\ldots n\\
\left\{\Psi\right\} &= \begin{bmatrix} u \\ v \end{bmatrix} = \begin{bmatrix} S_j & 0 & S_j & \cdots & 0 & S_j & 0 \\ 0 & S_j & 0 & \cdots & S_j & 0 & S_j \end{bmatrix} \begin{Bmatrix} u_j \\ v_j \end{Bmatrix}, \quad j = 1 \ldots\ldots n\\
\left\{\Psi\right\} &= \left[S\right]\left\{d^{(e)}\right\}
\end{aligned}
\tag{18}
$$

where: $\left\{d^{(e)}\right\}$ is $2m\times1$ the vector of nodal displacements of the element, while $m = 6$ *or* 10 nodes in each triangular element, $[S]$ is the $(2\times2\ m)$ matrix of displacement shape functions,

Here, the total potential energy function π_p, the total strain energy U, and the potential energy of surface tractions Ω_s are written as:

$$
\begin{aligned}
\pi_p &= U - \Omega_s\\
U &= \frac{1}{2}\int_V \left\{\varepsilon-\varepsilon_T\right\}^T \left\{\sigma\right\} dV\\
\Omega_s &= \int_S \left\{\Psi_s\right\}^T \left\{f\right\} dS
\end{aligned}
\tag{19}
$$

where: $\{f\}$ is the surface tractions, and $\{\Psi_s\}$ represents the field of surface displacements.
The total potential energy function can be rewritten as:

$$
\begin{aligned}
\pi_p &= \frac{1}{2}\int_V \left\{\varepsilon-\varepsilon_T\right\}^T \left\{\sigma\right\} dV - \int_S \left\{\Psi_s\right\}^T \left\{f\right\} dS\\
\left\{\Psi_s\right\} &= \left[S_s\right]\left\{d^{(e)}\right\}
\end{aligned}
\tag{20}
$$

where: V is the volume of the element, $\{\Psi_s\}$ is the field of surface displacements on which the surface tractions act.

Substituting Eq. (18) into Eq. (3), the isotropic strain and stress relations can be expressed in matrix form in terms of the nodal displacement vector $\left\{d^{(e)}\right\}$ by differentiating suitably as:

$$
\begin{aligned}
\left\{\varepsilon\right\} &= \begin{bmatrix} \varepsilon_{rr} \\ \varepsilon_{\theta\theta} \\ \gamma_{r\theta} \end{bmatrix} = \left[B^{(s)}\right]\left\{d^{(e)}\right\}\\
\left\{\sigma\right\} &= \left[D^{(s)}\right]\left(\left\{\varepsilon\right\}-\left\{\varepsilon_T\right\}\right)\\
&= \left[D^{(s)}\right]\left[B^{(s)}\right]\left\{d^{(e)}\right\} - \left[D^{(s)}\right]\left\{\varepsilon_T\right\}
\end{aligned}
\tag{21}
$$

where: $[B^{(s)}]$ represents the derivatives of the shape functions in the plane strain problem, and $\left[D^{(s)}\right]$ is given in Eq. (3). The potential energy of the typical elements, which can be written as:

$$\begin{aligned}\pi_p &= \frac{1}{2}\iiint_V \left\{d^{(e)}\right\}^T \left[B^{(s)}\right]^T \left[D^{(s)}\right]\left[B^{(s)}\right]\left\{d^{(e)}\right\}dV \\ &-\frac{1}{2}\iiint_V \left\{d^{(e)}\right\}^T \left[B^{(s)}\right]^T \left[D^{(s)}\right]\{\varepsilon_T\}dV - \int_\Gamma \left\{d^{(e)}\right\}[N]^T \{f\}dS\end{aligned} \tag{22}$$

On minimizing the potential energy, the stiffness matrix can be expressed as an integral over the volume or area along a specific length, and the load vectors due to temperature change as:

$$\begin{aligned}[K_s] &= \int_A \left(\left[B^{(s)}\right]^T \left[D^{(s)}\right]\left[B^{(s)}\right]\right) r\,dr d\theta \\ \{f_T\} &= \iiint_V \left[B^{(s)}\right]^T \left[D^{(s)}\right]\{\varepsilon_T\}dV\end{aligned} \tag{23}$$

The equilibrium equations that describe the behavior of an element become:

$$\left[K_s^{(e)}\right]\left\{d^{(e)}\right\} = \{f_T\} \tag{24}$$

The global equations are derived by assembling the element matrices as follows:

$$\begin{aligned}&[K_s]^G \{d\} = \{F\}^G \quad \text{where} \\ &[K_s]^G = \left(\sum_{e=1}^{NE}\left[K_s^{(e)}\right]\right), \quad \{F\}^G = \sum_{e=1}^{NE}\left[f_{T(e)}\right] + \sum_{e=1}^{NE}\left[f_{s(e)}\right]\end{aligned} \tag{25}$$

The following linear system equation of the whole structure can be written in the following block matrix form

$$\begin{bmatrix} [K_s]^G & [-I] \\ [M_{Cd}] & [M_{CF}] \end{bmatrix}_{4N\times 4N} \begin{Bmatrix} \{d\} \\ \{F\}^G \end{Bmatrix}_{4N\times 1} = \begin{Bmatrix} \{O_{n\times 1}\} \\ \{dO\} + \{fO\} \end{Bmatrix}_{4N\times 1} \tag{26}$$

where: $[M_{Cd}]$, $[M_{CF}]$ are $2N\times 2N$ boundary conditions for nodal forces taking into account the force acting on nodes, $[K_s]^G$ is the global stiffness matrix, $[I]$ is the identity matrix, $\{O\}$ is the zero vector, $\{d\}$ and $\{F\}^G$ are the displacements and forces nodal column matrices, the $\{dO\}$ is $2N\times 1$ has zeros values for unknown values of nodal displacement and $\{fO\}$ is $2N\times 1$ has the known values of the nodal force and zero for unknown values, and N is the number of nodes in the global matrix.

The system of algebraic equations involving stiffness and boundary matrices can be utilized to solve any non-axisymmetric problem, accommodating various force conditions in polar coordinates. This system aims to determine the values of nodal displacements with a $2N\times 1$ size.

The methodology for solving the non-axisymmetric thermoelastic analysis of an FGM hollow cylinder is shown in the flowchart (Figure 3). The flowchart illustrates the steps from problem definition, material modeling, and finite element discretization, through thermal and thermoelastic analysis, to post-processing and verification.

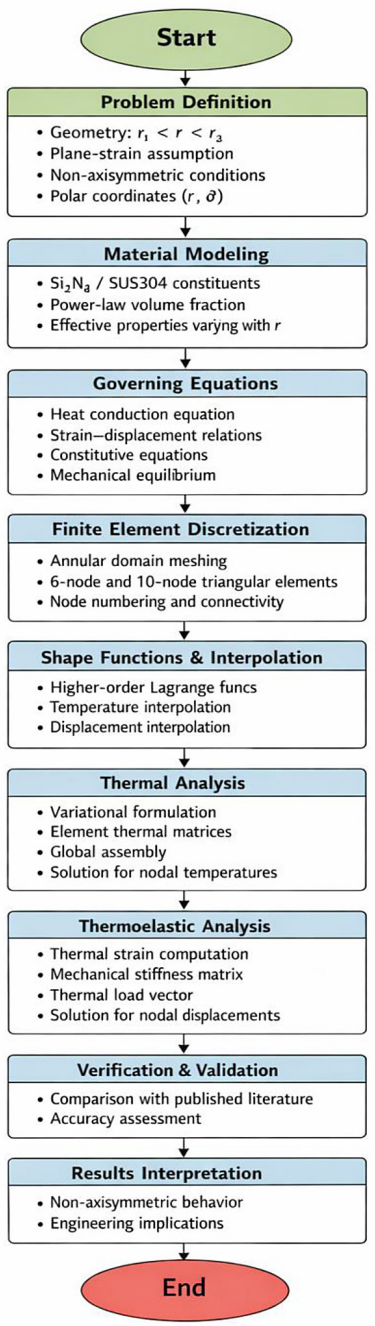

Figure 3. The flowchart of an FGM hollow cylinder analysis

NUMERICAL RESULTS

Verification problem

The thermal boundary conditions, material power-law index, and thermoelastic behaviors on the FGM hollow cylinder were analyzed using higher-order finite elements with 6 and 10-nodes. The cylinder has an inner radius of r_i = 0.25 m and an outer radius of r_o = 0.5 m, with a power-law index of n = 5. The inner surface is composed of silicon nitride (Si_3N_4), while the outer surface is made of stainless steel (SUS304). Material parameters are adopted from Table 1 in Xie et. al. (2013). For this verification problem, consider a hollow cylinder where the thermal boundary conditions are represented by the temperature distribution at the inner surface, which can be expressed as Xie et. al. (2013):

$$T(r_i, \theta) = 60 \cos(2\theta)\ ^\circ\text{C},$$
$$T(r_o, \theta) = 0\ ^\circ\text{C}. \tag{27}$$

Figure 4 depict the three-dimensional temperature distributions obtained through the implementation of 6 and 10-node triangular elements, respectively. The temperature distribution at both the inner and outer surfaces conforms to the associated boundary conditions, with maximum values observed at the inner surface. Subsequently, Figure 5 show profiles of three-dimensional radial and circumferential displacements for 6 nodes. Figure 6 show profiles of three-dimensional radial and circumferential displacements for 10-node triangular elements, respectively, due to the temperature variation. The thermal analysis verification procedure studied the effect of applying different triangular elements with 6 and 10 nodes on the temperature distribution in the problem under consideration. The shape functions presented in Eq. (17) were used in this analysis. The suitable aspect ratio for the 6-node triangular element is considered when the annulus domain is discretized as 36 lines along the r-direction and 11 curves in the r-direction. This discretization process yields 33 wedges, 792 nodes, 180 elements, and thus the global matrix for the whole structure becomes 1584×1584.

These figures reveal that the displacement components manifest as cosine waves along the circumferential direction, influenced by the cosine function applied at the inner surface. Furthermore, it is evident from Figures 5a and 6b that the maximum and minimum displacement values are almost equivalent for 6 and 10-nodes triangular elements. As depicted in Figure 7, the effect of increasing the volume fraction exponent n when $n \geq 1$ on the FGM hollow cylinder demonstrates an inverse relationship with radial displacement, resulting in a decrease in its values.

To validate the present results, a comparison is made between the results is related to the heat transfer equation with non-axisymmetric plan strain theory, respectively. Xie et. al. (2013) investigated the non-axisymmetric thermoelastic

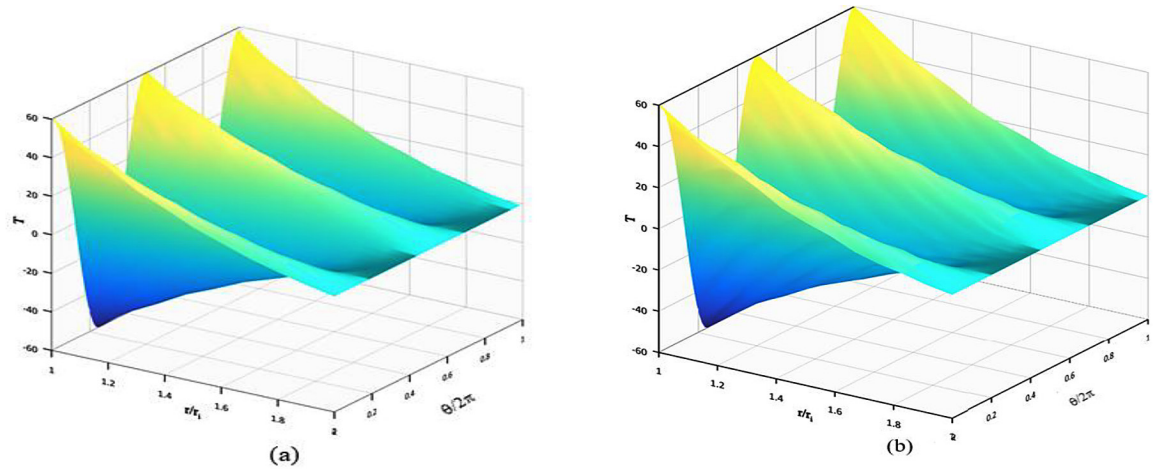

Figure 4. Three-dimensional temperature distribution in hollow FGM cylinder using: (a) 6-node triangular elements, (b) 10-node triangular elements

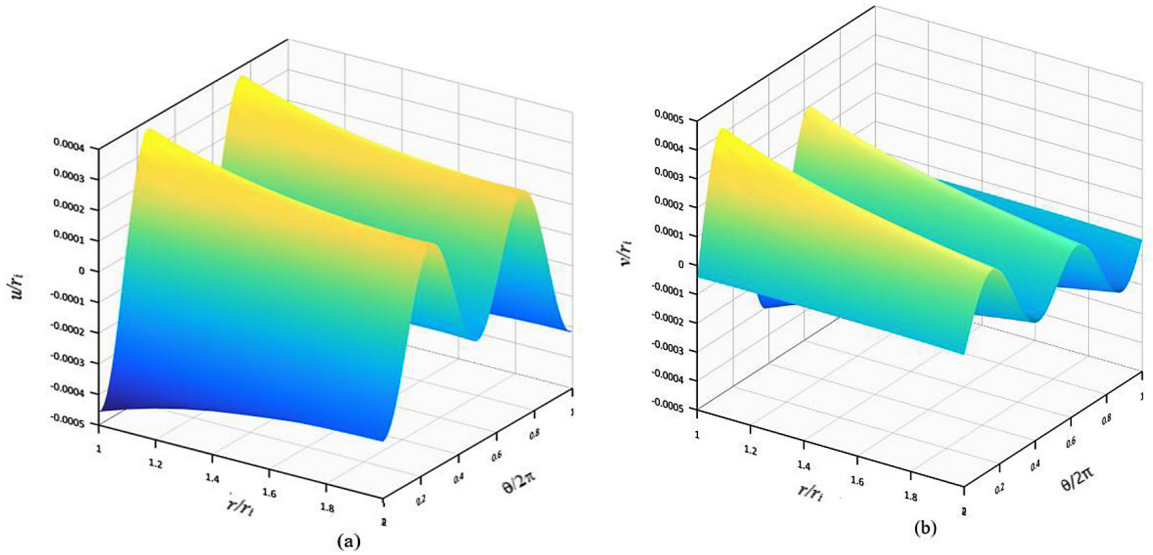

Figure 5. Variation of displacements in the hollow FGM cylinder applying 6-node triangular elements: (a) radial displacement, (b) circumferential displacement

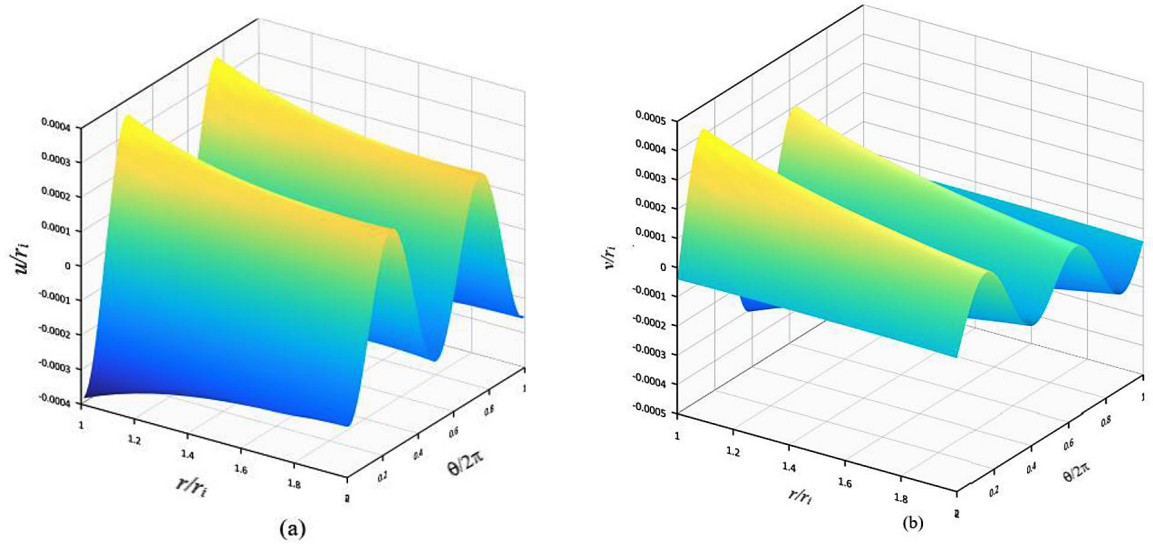

Figure 6. Three-dimensional in the cross-section of the FGM hollow cylinder with a ten-node triangular element: (a) radial displacement, (b) circumferential displacement

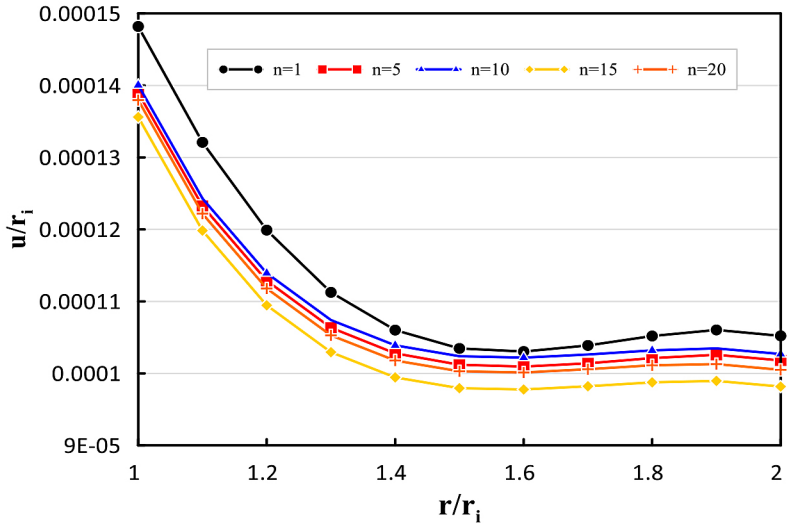

Figure 7. Radial displacement along the normalized radial direction at $\theta = \pi/3$ using the 6-node element for different values of FG index n

analysis of the FG hollow cylinder. So, the present results of the linear algebraic system will be validated with their results. These authors used a hollow cylinder that was subjected to a harmonic temperature distribution at the inner surface, as an oscillation of a cosine wave. However, the outside boundary is assumed to have zero temperature. Whereas the boundary conditions for displacements were assumed $u(b, \theta) = 0$, $v(b, \theta) = 0$, Xie et. al. (2013) solved the governing equations of the heat and plan strain equations by utilizing FDM under free traction force. The results of temperature distribution over the annulus presented in Figure 4 are compared with the results presented by Xie et al. (2013) (Figure 8). It is observed that the temperature distribution at the inner and outer surfaces satisfies the associated boundary conditions and has maximum values at the inner surface. Additionally, from the figures, it could be noticed that the temperature distribution of the 10-node triangular element is the closest to that of Xie et al. (2013). The non-axisymmetric plain strain analysis is represented mainly the variation of displacement due to the thermal effect and compared with Xie et al. (2013). the surfaces plotted in Figures 5 and 6 imply that the maximum values and minimum are equal, it can be observed that using higher-order elements can significantly improve the displacement results by increasing node numbers, that is by using 10 nodes exhibit good results and become closer to the results shown in Figures 9 and 10. However, the effect of using higher-order elements was presented extremely in circumferential displacement because of the functional load of temperature that was subjected as a function of a cosine wave. In Figure 7, the effect of increasing volume fraction exponent n when $n \geq 1$ on FGM hollow cylinder has an inverse relation with radial displacement which decreases in their value. It can be observed further that by increasing the number of nodes in elements the values of the radial displacement became smaller than the values shown in Xie et al. (2013). This helps to control the displacement depending on the application.

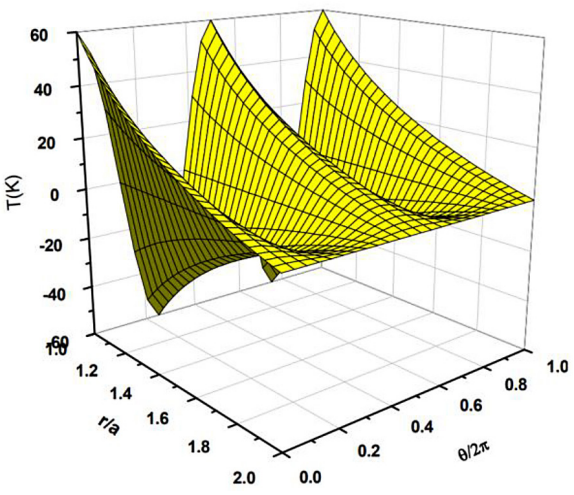

Figure 8. Three-dimensional temperature distribution in the cross-section of the FGM hollow cylinder in Xie et al. (2013)

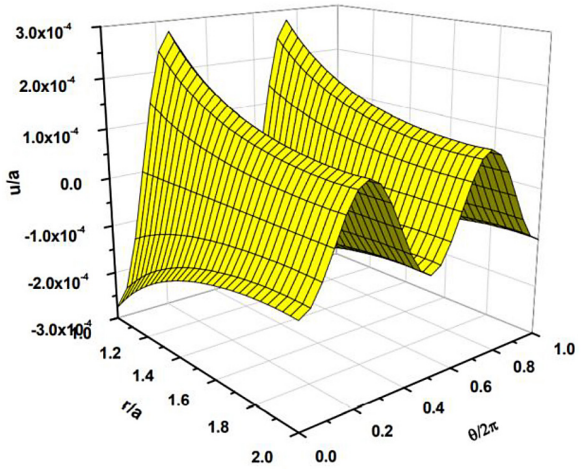

Figure 9. Three-dimensional radial displacement in the cross-section of the FGM hollow cylinder in Xie et al. (2013)

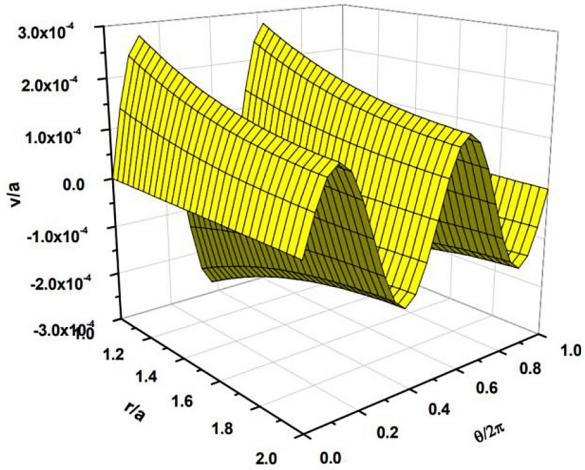

Figure 10. Three-dimensional circumferential displacement in the cross-section of the FGM hollow cylinder in Xie et al. (2013)

Example problem

The effect of non-axisymmetric variable temperature boundary conditions of an FGM hollow cylinder with $n = 5$ is investigated. The temperature boundary conditions are expected to be specified at the inner and outer surfaces of the annulus as:

$$T(r_i, \theta) = \begin{cases} 70\cos(2\theta)\ ^oC & \text{for } 0 \le \theta \le \pi \\ 100\cos(2\theta)\ ^oC & \text{for } \pi < \theta \le 2\pi \end{cases}$$

$$T(r_o, \theta) = 25\cos(2\theta)\ ^\circ\text{C}. \qquad (28)$$

Figure 11 illustrate the three-dimensional temperature distributions for 6 and 10-node triangular elements, respectively. The study showed that the inner surface is subjected to the two harmonic oscillations with varying amplitudes of thermal loads, i.e., the bottom section of the inner surface experiences an amplitude of 100, while the upper section encounters an amplitude of 70. At the outer surface, a harmonic oscillation with an amplitude of 25 is observed. Figure 12 illustrate the variation of temperature in the normalized hoop direction for different values of (r/r_i) using the 6 and 10-node triangular elements, respectively. From the curves of Figures 12 at the inner surface $r/r_i = 1$, it can be observed that there is a sharp increase in the temperature from 70 to 100 °C at $\theta/2\pi = 0.5$ which is due to the applied boundary conditions, Eq. (28). However, this sharp increase reduces

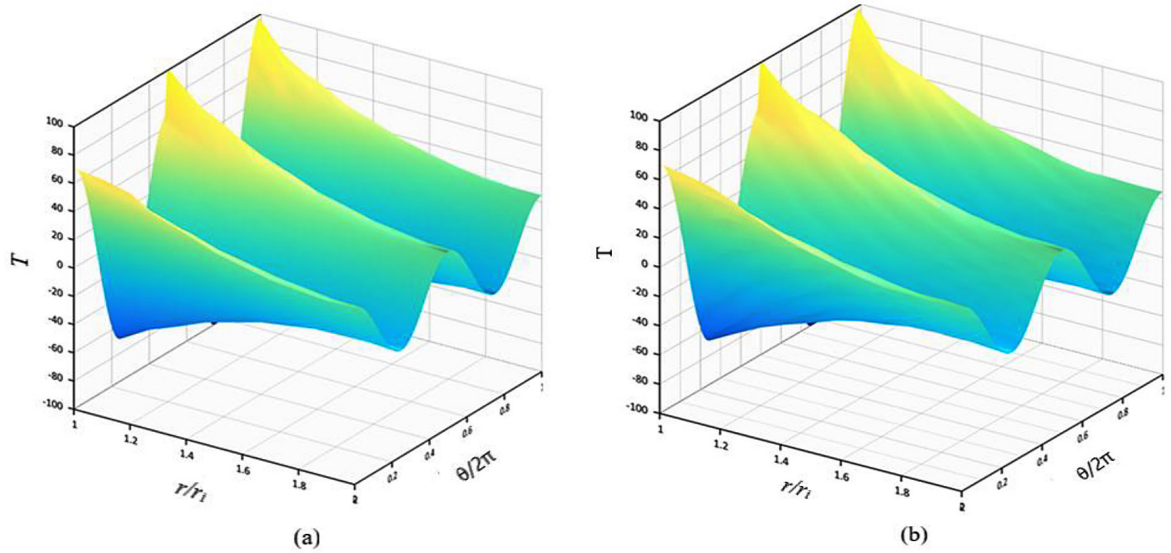

Figure 11. Three-dimensional temperature spreading in the cross-section of the FGM hollow cylinder: (a) 6-node triangular element, (b) 10-node triangular element

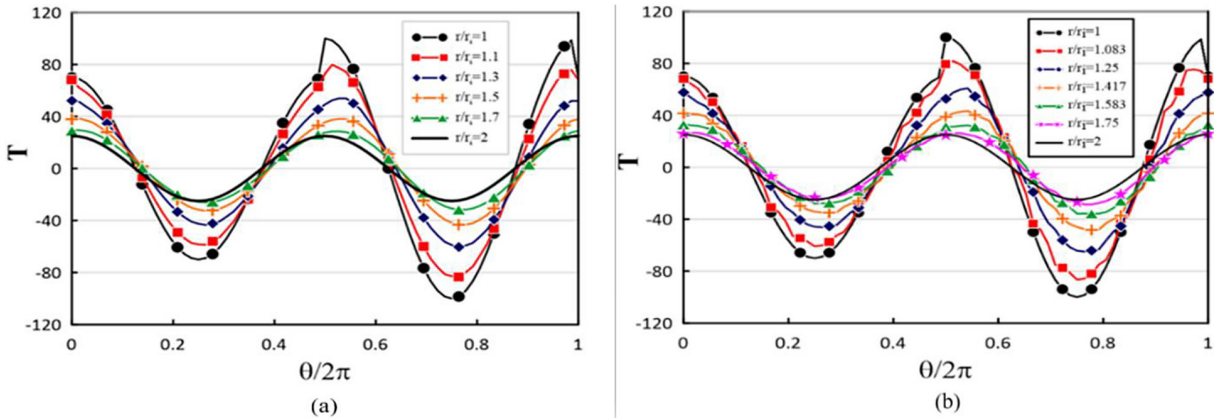

Figure 12. Variation of temperature in the normalized hoop-direction for different values of (r/r_i): (a) 6-node triangular element, (b) 10-node triangular element

smoothly as moving forward to the outer surface to reach the applied outer oscillation cosine wave of temperature. Furthermore, these figures demonstrate that the temperature adheres to the applied boundary conditions, with the temperature decreasing as r increases. Figures 13 and 14 depict profiles of three-dimensional radial and circumferential displacement for 6 and 10-node triangular elements due to the given temperature variations given in Eq. 28, respectively. It can be observed from Figures 13a and 14a that the resulting radial displacement behaves as a cosine wave as the applied load at the inner and outer boundaries. Figures 13b and 14b illustrate the three-dimensional circumferential displacement of the FGM hollow cylinder using the 6 and 10-node elements, respectively. The curves indicate that the circumferential displacement exhibits a sinusoidal waveform, contrasting with both the radial displacements and the temperature applied at the inner and outer surfaces. Figures 15 and 16 show the distribution of the radial and circumferential displacement along the normalized circumferential direction ($\theta/2\pi$) at all annulus radii for 6 and 10-node triangular elements under consideration of thermal boundary conditions. Figures 13a and 14b show that the radial and circumferential displacement for 6 and 10 triangular elements satisfy the associated boundary conditions through the θ-direction.

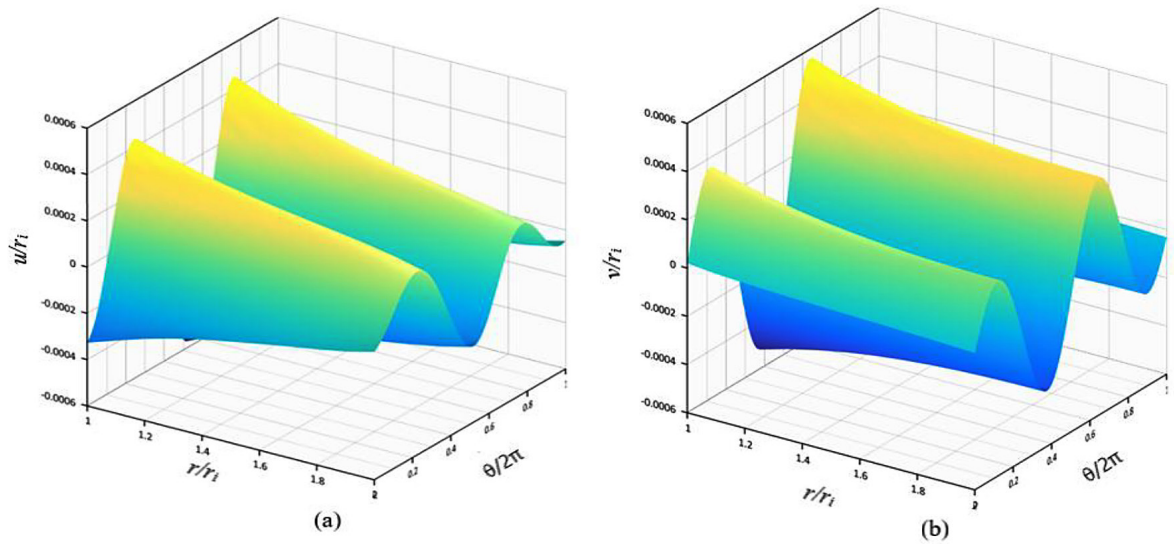

Figure 13. Three-dimensional in the cross-section of the FGM hollow cylinder with 6-node triangular element: (a) normalized radial displacement, (b) normalized circumferential displacement

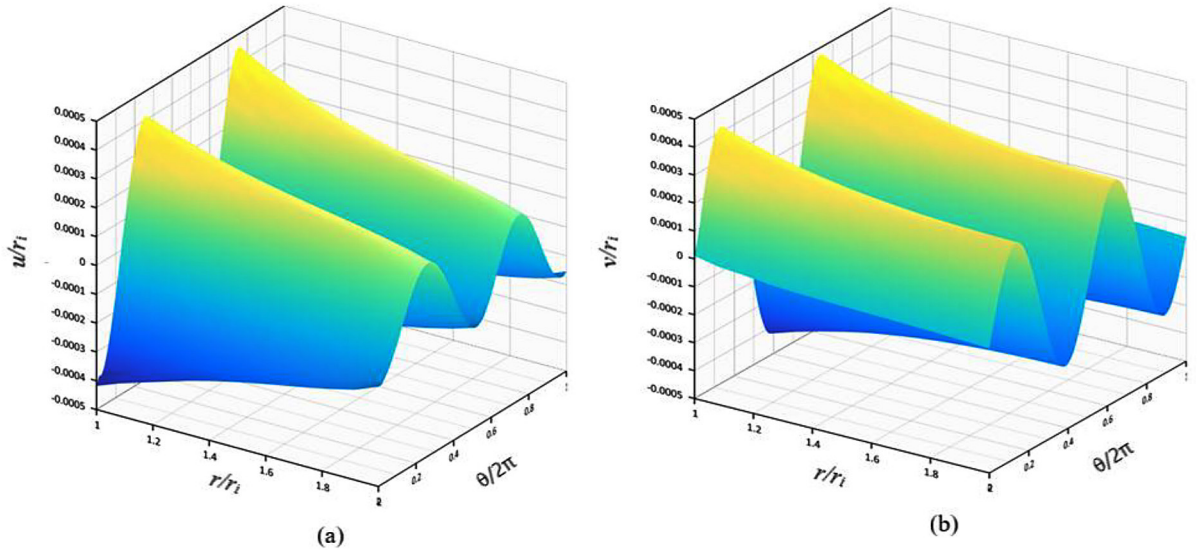

Figure 14. Three-dimensional in the cross-section of the FGM hollow cylinder with ten-node triangular element: (a) normalized radial displacement, (b) normalized circumferential displacement

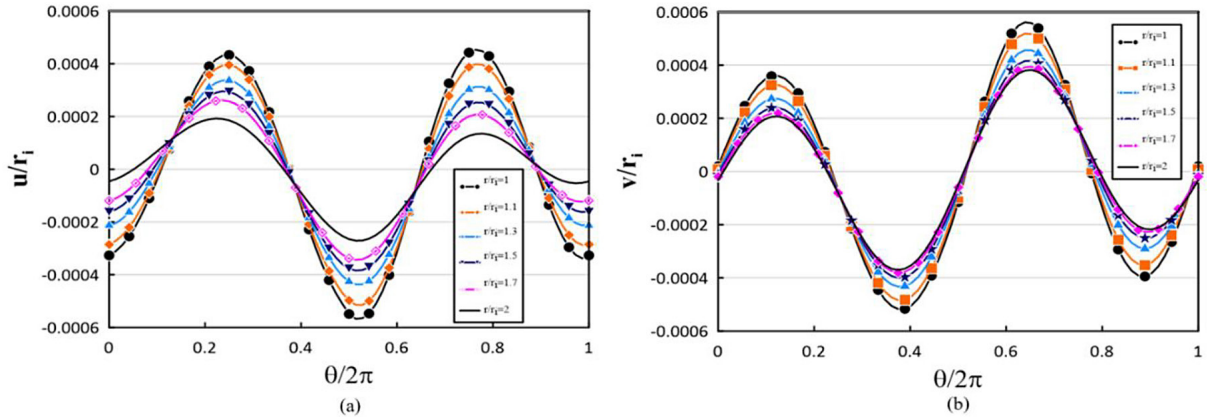

Figure 15. Variation for different values of (r/r_i) using six nodes triangular element between: (a) normalized radial displacement, (b) normalized hoop-direction

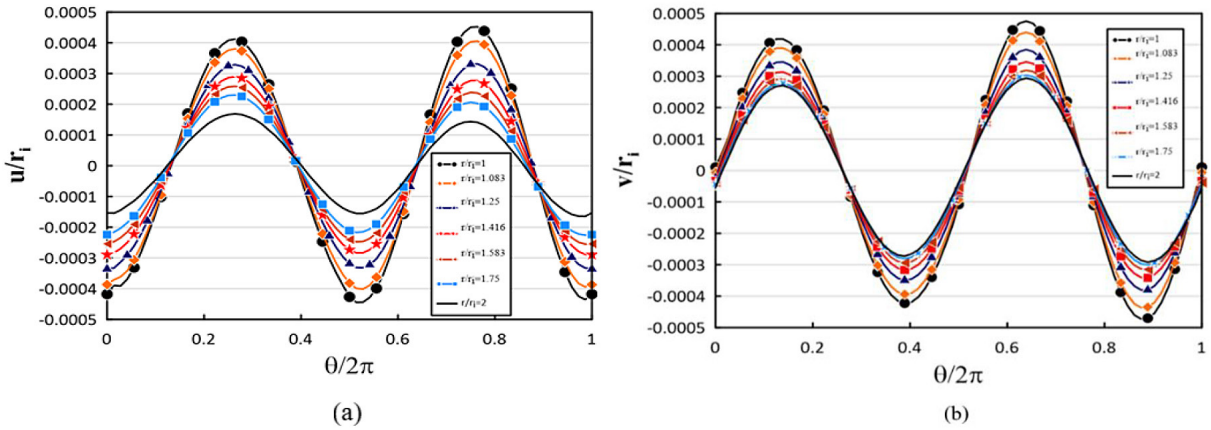

Figure 16. Variation for different values of (r/r_i) using ten nodes triangular element between (a) normalized radial displacement and (b) normalized hoop-direction

Table 2. List of nomenclature

Symbol	Name
E	Young's modulus
G	Shear modulus of elasticity
K	Bulk module
k	Thermal conductivity
ν	Poisson ratio
n	Power law gradient index
P	Material properties
P_m, P_C	Metal, and *ceramic properties*
(r, θ)	Radial direction and circumferential direction
$T\,(r, \theta)$	Temperature distribution in polar coordinates
Vc, Vm	Volume fraction of ceramic and metal
$\dot{q}$	Heat generation
$[S]$	The matrix of the shape function
Aj, Bj, Dj	Arbitrary constants of the interpolation function
$\varepsilon_{rr}, \varepsilon_{\theta\theta}, \varepsilon_{r\theta}, \varepsilon_T$	radial, circumferential, shear, thermal strains
$\sigma_{rr}, \sigma_{\theta\theta}, \tau_{r\theta}$	Radial, circumferential, and shear stresses
$(c_{11}, c_{12}, c_{21}, c_{22}, c_{33})$	Elastic stiffness coefficients
c_T	Thermal stiffness coefficients
$(C_{11}, C_{12}, C_{21}, C_{22})$	conduction and convection coefficients
$\zeta_i(\theta), \zeta_o(\theta)$	known temperature distributions at the boundary of the hollow cylinder
$\{T^e\}$	The nodal temperature matrix
Ω	Element volume domain
Γ	Element surface boundary
$[D]$	Material property matrix
$[B]$	The derivatives of the shape functions matrix
$[X_1]$, $[X_2]$	Boundary conditions related to nodal temperature and nodal forces of heat equation
$\{\varphi\}$	Known temperature and nodal forces satisfying any given boundary conditions
$[I]$	Identity matrix
$\{O\}$	Zero vector
$[K_c]^G$	Global stiffness matrix
$S_{f_{bound}}$	The area where heat flux is applied
π_p, π_h	Total potential energy function
U, Ω_s	Total strain energy and the potential energy of surface tractions
[MCd], [MCF]	Boundary conditions matrix related to plane strain
$\{dO\}$	Nodal displacement vector
$\{fO\}$	Nodal force vector
$\{d\}$	Displacement vector
(u, v)	Radial and circumferential displacements
N	Number of nodes in the global matrix
α	Thermal expansion coefficient
ρ	Mass density

CONCLUSIONS

In this study, the variational approach was employed with a higher-order triangular element with 6- and 10-nodes to solve the linear algebraic system that includes the non-axisymmetric thermoelastic performance of an FGM hollow cylinder exposed to variable hoop temperature. A strong agreement was achieved when a comprehensive comparison of the thermal and displacement distributions across the cylinder's annulus was conducted. The result showed that triangular elements with 10 nodes are more accurate than 6 nodes in the heat transfer analysis to approach the exact solution. Moreover, the heat distribution and the radial displacement follow a linear function and a zero value in circumferential displacement when the thermal load is assumed constant and uniform at the inner surface. This study also examined the impact of the volume-graded index on heat and displacement variations along the radial direction. This study found that increasing the volume fraction exponent n when n ≥ 1 on the FGM hollow cylinder demonstrates an inverse relationship with radial displacement. The volume graded index has a great significant effect on the heat and displacement variations through the radial direction. For increasing the volume exponent index, the radial displacement decreases.

Therefore, it is recommended for the future to study the stress of non-axisymmetric thermoelastic behavior of FGM hollow cylinder by implementation with higher-order FEM in a high-temperature application.

REFERENCES

1. Asgari, M., and Akhlaghi, M. Transient thermal stresses in two dimensional functionally graded thick hollow cylinder with finite length. Heat Mass Transfer, 2009, 45: 1383–1392. https://doi.org/10.1007/s00419-009-0321-2.
2. Benslimane, A., Methia, M., Khadimallah, M., and Hammiche, D., Stress analysis of rotating thick-walled nonhomogeneous sphere under thermomechanical loadings. Forces in Mechanics, 2023, 11. https://doi.org/10.1016/j.finmec.2023.100183.
3. Darabseh, T. and Alshaer, B., and Khrais, S. Thermoelastic analysis of 2D-FGM hollow circular cylinder with finite length by finite element method. International Journal Computer Applications in Technology, 2013, 46(2): 175-186. https://doi.org/10.1504/IJCAT.2013.052297.

4. Dai, H., Rao, Y., and Dai, T. A review of recent researches on FGM cylindrical structures under coupled physical interactions, 2000–2015. Composite Structures, 2016, 152: 199-225. https://doi.org/10.1016/j.compstruct.2016.05.042.
5. Eldeeb, A., Shabana, Y., El-Sayed, T., Guo, L., and Elsawaf, A. Thermoelastic stresses alleviation for two-dimensional functionally graded cylinders under asymmetric loading. Journal of Thermal Stresses, 2023, 46: 59–74. https://doi.org/10.1080/01495739.2022.2151960.
6. Eldeeb, AM., Shabana, YM., and Elsawaf, A. Thermo-elastoplastic behavior of a rotating sandwich disc made of temperature-dependent functionally graded materials. Journal of Sandwich Structures & Materials, 2020, 23. https://doi.org/10.1177/1099636220904970
7. Eldeeb, AM., Shabana, YM., and Elsawaf, A. Investigation of the thermoelastoplastic behaviors of multilayer FGM cylinders. Composite Structures, 2021, 276. https://doi.org/10.1016/j.compstruct.2021.114523
8. Farukoğlu, Ö, Korkut, I., and Motameni, A. (), Comprehensive elastic analysis of functionally graded variable thickness pressurized disk. Journal of Applied Mathematics and Mechanics (Zeitschrift für Angewandte Mathematik und Mechanik), 2023, 103. https://doi.org/10.1002/zamm.202200506
9. Golzari, A. and Asgari, M. Dynamic analysis and wave propagation in rotating heterogeneous cylinders under moving load and thermal conditions: Implementing an efficient mesh free method. Applied Mathematical Modelling, 2018, 61: 377-407. https://doi.org/10.1016/j.apm.2018.05.001.
10. Hosseini, S., Akhlaghi, M., and Shakeri, M. Transient heat conduction in functionally graded thick hollow cylinders by analytical method, Heat and Mass Transfer, 2007, 43: 669–675. https://doi.org/10.1007/s00231-006-0158-y
11. Jabbari, M., Bahtui, A., and Eslami, M. Axisymmetric mechanical and thermal stresses in thick short length FGM cylinders. International Journal of Pressure Vessels and Piping, 2009, 86: 296-306. https://doi.org/10.1016/j.ijpvp.2008.12.002
12. Jabbari, M., Sohrabpour, S., and Eslami, M. General solution for mechanical and thermal stresses in a functionally graded hollow cylinder due to nonaxisymmetric steady-state loads. Journal of Applied Mechanics, 2003, 70: 111-118. https://doi.org/10.1016/S0308-0161 (02)00043-1
13. Najibi, A. Mechanical stress reduction in a pressurized 2D-FGM thick hollow cylinder with finite length. International Journal of Pressure Vessels and Piping, 2017, 153: 32-44. https://doi.org/10.1016/j.ijpvp.2017.05.007
14. Najibi, A. and Talebitooti, R. Nonlinear transient thermo-elastic analysis of a 2D-FGM thick hollow finite length Cylinder, Composites Part B. 2017, 111: 211-227. https://doi.org/10.1016/j.compositesb.2016.11.055
15. Nayak, P., Bhowmick, S., and Saha, K. Elasto-plastic analysis of thermo-mechanically loaded functionally graded disks by an iterative variational method, Engineering Science and Technology, an International Journal, 2019, 23: 42-64. https://doi.org/10.1016/j.jestch.2019.04.007
16. Pany, C. and Parthan, S., Free vibration analysis of an orthogonally supported multi-span curved panel. Journal of Sound and Vibration, 2001, 241(2): 315–318. https:// doi:10.1006/jsvi.2000.3240.
17. Paul, V., Mehta, P., Sahni, M., and León-Castro, E. Numerical simulation of stresses in functionally graded hcs-mgo cylinder using iterative technique and finite element method. Materials, 2022, 15. https://doi.org/10.3390/ma15134537
18. Paul, S. and Sahni, M. Two-dimensional stress analysis of a thick hollow cylinder made of functionally graded material subjected to non-axisymmetric loading. Structural Integrity and Life, 2021, 21: S75–S81. https://doi.org/10.33889/IJMEMS.2021.6.4.066
19. Saadatfar, M. Transient solution of heat and moisture transfer in a functionally graded hollow cylinder with finite length. Mechanics of Advanced Composite Structure, 2022, 9(18): 49-57. https://doi.org/10.22075/macs.2022.24225.1355
20. Salehi, A., and Ahmadi, I. Transient thermal and mechanical stress analysis of 2D functionally
21. graded finite cylinder: A truly meshless formulation. Iranian Journal of Science and Technology, Transactions of Mechanical Engineering, 2022, 46: 573–598. https://doi.org/10.1007/s40997-021-00432-6
22. Shariyat, M. A nonlinear Hermitian transfinite element method for transient behavior analysis of hollow functionally graded cylinders with temperature-dependent materials under thermo-mechanical loads. International Journal of Pressure Vessels and Piping, 200, 86: 280–289. https://doi.org/10.1016/j.ijpvp.2008.09.004
23. Shao, Z., Ang, K., Reddy, J. and Wang, T. Nonaxisymmetric thermomechanical analysis of functionally graded hollow cylinders. Journal of Thermal Stresses, 2008, 31: 515–536. https://doi.org/10.1080/01495730801977879
24. Shojaeefard, M. and Najibi, A. Nonlinear transient heat conduction analysis of hollow thick temperature-dependent 2D-FGM cylinders with finite length using numerical method. Journal of Mechanical Science and Technology, 2014, 28: 3825–3835. https://doi.org/10.1007/s12206-014-0846-3.
25. Sharma, D., and Kaur, R. Thermoelastic analysis of FGM hollow cylinder for variable parameters

and temperature distributions using FEM. Nonlinear Engineering, 2020, 9: 256–264. https://doi.org/10.1515/nleng-2020-0013.

26. Singh, S., Sondhi, L., Sahu, R., and Madan, R. Exploring the mechanical response of functionally graded hollow disks: insights from rotation, gravity, and variable heat generation. International Journal of Structural Integrity, 2024, 15(1): 97-119. https://doi.org/10.1108/IJSI-10-2023-0095.
27. Sreeju Nair S., Pany, C. Functionally graded panels: A review. International Journal for Modern Trends in Science and Technology, 2020, 6(8): 36-43. https://doi.org/10.46501/IJMTST060808.
28. Tang, Y. Heat transfer and thermal analysis with computational fluid dynamics. IntechOpen, 2024. https://doi.rg/10.5772/intechopen.1006819.
29. Xie, H., Dai, H. and Rao, Y. Thermoelastic dynamic behaviors of a fgm hollow cylinder under non-axisymmetric thermo-mechanical loads. Journal of Mechanics, 2013, 29: 109– 120. https://doi.org/10.1017/jmech.2012.112
30. Yıldırım, V. Exact thermal analysis of functionally graded cylindrical and spherical vessels. International Journal of Engineering & Applied Sciences, 2017, 9: 112-126. https://doi.org/10.24107/ijeas.318459.